Available online at www.sciencedirect.com
ScienceDirect
Journal of Power Sources 161 (2006) 628–639
JOURNAL OF POWER SOURCES
www.elsevier.com/locate/jpowsour

# Solid-state diffusion limitations on pulse operation of a lithium ion cell for hybrid electric vehicles

Kandler Smith, Chao-Yang Wang *

*Electrochemical Engine Center (ECEC), and Department of Mechanical Engineering, The Pennsylvania State University, University Park, PA 16802, USA*

Received 21 December 2005; received in revised form 15 March 2006; accepted 28 March 2006
Available online 11 May 2006

**Abstract**

A 1D model based on physical and electrochemical processes of a lithium ion cell is used to describe constant current and hybrid pulse power characterization (HPPC) data from a 6 Ah cell designed for hybrid electric vehicle (HEV) application. An approximate solution method for the diffusion of lithium ions within active material particles is formulated using the finite element method and implemented in the previously developed 1D electrochemical model as an explicit difference equation. Reaction current distribution and redistribution processes occurring during discharge and current interrupt, respectively, are driven by gradients in equilibrium potential that arise due to solid diffusion limitations. The model is extrapolated to predict voltage response at discharge rates up to 40 C where end of discharge is caused by negative electrode active material surface concentrations near depletion. Simple expressions are derived from an analytical solution to describe solid-state diffusion limited current for short duration, high-rate pulses.


*Keywords:* Lithium ion battery; Electrochemical modeling; Hybrid electric vehicle; Transient; Solid-state diffusion

## 1. Introduction

Hybrid electric vehicles (HEVs) use a battery as a high-rate transient power source cycled about a relatively fixed state-of-charge (SOC). In the literature however, most fundamentally based battery models focus on predicting energy available at various constant current discharge rates beginning from the fully charged state [1–3]. Cell phone, laptop, and electric vehicle batteries are typically discharged over some hours and it is common in the literature to term discharge rates of only 4 C (four times the manufacturer's nominal one hour Ah rating, lasting on the order of 15 min) as "high-rate". In contrast, Hitachi states that their 5.5 Ah HEV cell can sustain 40 C discharge from 50% SOC for greater than 5 s. Phenomenological models capable of capturing ultra-high-rate transient behavior are needed to understand and establish the operating limitations of HEV cells.

In the mathematical modeling of HEV cells, equivalent circuit models are often employed [4–7] and validated in either the time or frequency domain [8–10]. While the simplicity of such models makes them attractive, unlike fundamental models they provide no insight into underlying physical cell limitations. Many good works do exist in the fundamental modeling of lithium ion cells, though validated models are only available for cell phone, laptop, and electric vehicle batteries. We briefly outline some of those works.

Doyle et al. [11] developed a 1D model of the lithium ion cell using porous electrode and concentrated solution theories. The model is general enough to adopt a wide range of active materials and electrolyte solutions with variable properties and has been applied in various studies [1,2,12–14]. In [1], Doyle et al. validated the model against constant current data (with rates up to 4 C) from similar cells of three different electrode thicknesses. Solid and electrolyte phase mass transport properties were estimated to fit measured data, and in particular, the solid diffusion coefficient for $Li_xC_6$ ($D_{s-} = 3.9 \times 10^{-10}$ cm$^2$ s$^{-1}$) was chosen to capture rate dependent end of discharge. Interfacial resistance was used as an adjustable parameter to improve the model's fit across the three cell designs. More recently, the 1D isothermal model was validated against a 525 mAh Sony cell phone battery [2]. The authors used a large Bruggeman exponent correcting for

* Corresponding author. Tel.: +1 814 863 4762; fax: +1 814 863 4848.
*E-mail address:* cxw31@psu.edu (C.-Y. Wang).

0378-7753/$ – see front matter © 2006 Elsevier B.V. All rights reserved.
doi:10.1016/j.jpowsour.2006.03.050

**Nomenclature**

| | |
|---|---|
| $a_s$ | active surface area per electrode unit volume ($cm^2\ cm^{-3}$) |
| $A$ | electrode plate area ($cm^2$) |
| **A** | state matrix in linear state variable model state equation |
| **B** | input matrix in linear state variable model state equation |
| $c$ | concentration of lithium in a phase ($mol\ cm^{-3}$) |
| **C** | state matrix in linear state variable model output equation |
| $D$ | diffusion coefficient of lithium species ($cm^2\ s^{-1}$) |
| **D** | input matrix in linear state variable model output equation |
| $F$ | Faraday's constant (96,487 C $mol^{-1}$) |
| $i_0$ | exchange current density of an electrode reaction ($A\ cm^{-2}$) |
| $I$ | applied current (A) |
| $j^{Li}$ | reaction current resulting in production or consumption of Li ($A\ cm^{-3}$) |
| $L$ | width (cm) |
| $p$ | Bruggeman exponent |
| $Q$ | capacity (A s) |
| $r$ | radial coordinate (cm) |
| $R$ | universal gas constant (8.3143 J $mol^{-1}\ K^{-1}$) |
| $R_f$ | film resistance on an electrode surface ($\Omega\ cm^2$) |
| $R_s$ | radius of solid active material particles (cm) |
| $R_{SEI}$ | solid/electrolyte interfacial flim resistance ($\Omega\ cm^2$) |
| $s$ | Laplace variable ($rad\ s^{-1}$) |
| $t$ | time (s) |
| $t_+^0$ | transference number of lithium ion with respect to the velocity of solvent |
| $T$ | absolute temperature (K) |
| $T_s$ | time step (s) |
| $U$ | open-circuit potential of an electrode reaction (V) |
| $x$ | negative electrode solid phase stoichiometry and spatial coordinate (cm) |
| $y$ | positive electrode solid phase stoichiometry |

*Greek symbol*

| | |
|---|---|
| $\alpha_a, \alpha_c$ | anodic and cathodic transfer coefficients for an electrode reaction |
| $\delta$ | penetration depth (cm) |
| $\varepsilon$ | volume fraction or porosity of a phase |
| $\eta$ | surface overpotential of an electrode reaction (V) |
| $\kappa$ | conductivity of an electrolyte ($S\ cm^{-1}$) |
| $\kappa_D$ | diffusional conductivity of a species ($A\ cm^{-1}$) |
| $\sigma$ | conductivity of solid active materials in an electrode ($S\ cm^{-1}$) |
| $\tau$ | dimensionless time for solid-state diffusion |
| $\phi$ | volume-averaged electrical potential in a phase (V) |
| $\omega$ | frequency ($rad\ s^{-1}$) |

*Subscripts*

| | |
|---|---|
| e | electrolyte phase |
| s | solid phase |
| s,avg | average, or bulk solid phase |
| s,e | solid phase at solid/electrolyte interface |
| s,max | solid phase theoretical maximum limit |
| sep | separator region |
| − | negative electrode region |
| + | positive electrode region |

*Superscripts*

| | |
|---|---|
| eff | effective |
| Li | lithium species |

tortuosity in the negative electrode ($p = 3.3$) leading to the conclusion that the battery was electrolyte phase limited. Though the model successfully predicted end of discharge for rates up to 3 C, the voltage response during the first minutes of discharge did not match and was found to be sensitive to values chosen for interfacial resistances.

While the majority of the modeling literature is devoted to voltage prediction during quasi-steady state constant current discharge and charge, we note several discussions of transient phenomena relevant to HEV cells. Neglecting effects of concentration dependent properties (that generally change modestly with time), the three transient processes occurring in a battery are double-layer capacitance, electrolyte phase diffusion, and solid phase diffusion. Due to the facile kinetics of lithium ion cells, Ong and Newman [15] demonstrated that double-layer effects occur on the millisecond time scale and can thus be neglected for current pulses with frequency less than ~100 Hz.

Unlike double-layer capacitance, electrolyte and solid phase diffusion both influence low-frequency voltage response and the relative importance of various diffusion coefficient values can be judged either in the frequency domain [16,17] or through analysis of characteristic time scales [13,14]. Fuller et al. [14] studied the practical consequence of these transient phenomena by modeling the effect of relaxation periods interspersed between discharge and charge cycles of various lithium ion cells. Voltage relaxation and the effect of repeated cycling were influenced very little by electrolyte concentration gradients and were primarily attributed to equalization of local state of charge across each electrode. Non-uniform active material concentrations would relax via a redistribution process driven by the corresponding non-uniform open-circuit potentials across each electrode.

This work extends a previously developed 1D electrochemical model [3] to include transient solid phase diffusion and uses it to describe constant current, pulse current, and driving cycle test data from a 6 Ah lithium ion cell designed and built for the DOE FreedomCAR program. The model highlights several effects attributable to solid-state diffusion relevant to pulse operation of HEV batteries.

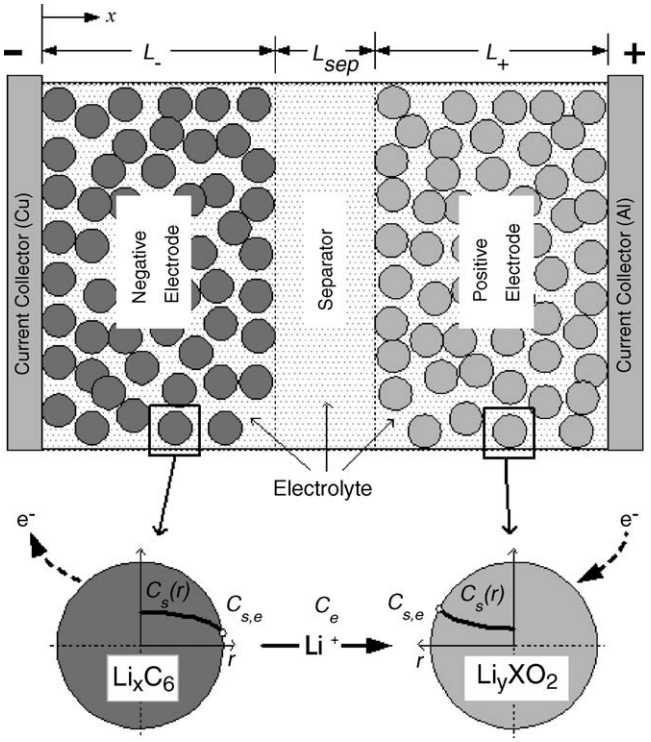


Fig. 1. Schematic of 1D ($x$-direction) electrochemical cell model with coupled 1D ($r$-direction) solid diffusion submodel.

## 2. Model formulation

The 1D lithium ion cell model depicted in Fig. 1 consists of three domains—the negative composite electrode (with $Li_xC_6$ active material), separator, and positive composite electrode (with a metal oxide active material). During discharge, lithium ions inside of solid $Li_xC_6$ particles diffuse to the surface where they react and transfer from the solid phase into the electrolyte phase. The positively charged ions travel via diffusion and migration through the electrolyte solution to the positive electrode where they react and insert into metal oxide solid particles. The separator, while conductive to ions, is an electronic insulator, thus forcing electrons to follow an opposite path through an external circuit or load.

The composite electrodes, consisting of active material and electrolyte solution (along with lesser amounts of conductive filler and binder, not shown in Fig. 1), are modeled using porous electrode theory, meaning that the solid and electrolyte phases are treated as superimposed continua without regard to microstructure. Electrolyte diffusion and ionic conductivity are corrected for tortuosity resulting from the porous structure using Bruggeman relationships, $D_e^{\text{eff}} = D_e\varepsilon_e^p$ and $\kappa^{\text{eff}} = \kappa\varepsilon_e^p$, respectively.

Electronic conductivity is corrected as a function of each electrode's solid phase volume fraction, $\sigma^{\text{eff}} = \sigma\varepsilon_s$. Mathematical equations governing charge and species conservation in the solid and electrolyte phases are summarized in Table 1.

Distribution of liquid phase potential, $\phi_e$, is described by ionic and diffusional conductivity, Eq. (1), with diffusional conductivity:

$$\kappa_D^{\text{eff}} = \frac{2RT\kappa^{\text{eff}}}{F}(t_+^0 - 1)\left(1 + \frac{\mathrm{d}\ln f_\pm}{\mathrm{d}\ln c_e}\right) \tag{5}$$

described by concentrated solution theory [3,11]. Distribution of solid phase potential, $\phi_s$, is governed by Ohm's law, Eq. (2). The reaction current density, $j^{\text{Li}}$, sink/source term appears with opposite signs in the charge conservation equations for the two phases, maintaining electroneutrality on both a local and global basis. Reaction rate is coupled to phase potentials by the Butler–Volmer kinetic expression:

$$j^{\text{Li}} = a_s i_0 \left\{\exp\left[\frac{\alpha_a F}{RT}\left(\eta - \frac{R_{\text{SEI}}}{a_s} j^{\text{Li}}\right)\right] - \exp\left[-\frac{\alpha_c F}{RT}\left(\eta - \frac{R_{\text{SEI}}}{a_s} j^{\text{Li}}\right)\right]\right\}, \tag{6}$$

with overpotential, $\eta$, defined as the difference between the solid and liquid phase potentials, minus the open-circuit potential of the solid or $\eta = \phi_s - \phi_e - U$. Exchange current density, $i_0$, exhibits modest dependency on electrolyte and solid surface concentrations, $c_e$ and $c_{s,e}$, respectively, according to $i_0 = (c_e)^{\alpha_a}(c_{s,\max} - c_{s,e})^{\alpha_a}(c_{s,e})^{\alpha_c}$. A resistive film layer, $R_{\text{SEI}}$, may be included to model a finite film at the surface of electrode active material particles which reduces the overpotential's driving force [18].

Solid-state transport of Li within spherical $Li_xC_6$ and metal oxide active material particles is described by diffusion, Eq. (4). Note that the macroscopic cell model requires only the value of

Table 1
Governing equations of lithium ion cell model

| Conservation equations | | | Boundary conditions |
|---|---|---|---|
| Charge | | | |
| Electrolyte phase | $\frac{\partial}{\partial x}\left(\kappa^{\text{eff}}\frac{\partial}{\partial x}\phi_e\right) + \frac{\partial}{\partial x}\left(\kappa_D^{\text{eff}}\frac{\partial}{\partial x}\ln c_e\right) + j^{\text{Li}} = 0$ | (1) | $\left.\frac{\partial\phi_e}{\partial x}\right\|_{x=0} = \left.\frac{\partial\phi_e}{\partial x}\right\|_{x=L} = 0$ |
| Solid phase | $\frac{\partial}{\partial x}\left(\sigma^{\text{eff}}\frac{\partial}{\partial x}\phi_s\right) - j^{\text{Li}} = 0$ | (2) | $-\sigma_-^{\text{eff}}\left.\frac{\partial\phi_s}{\partial x}\right\|_{x=0} = \sigma_+^{\text{eff}}\left.\frac{\partial\phi_s}{\partial x}\right\|_{x=L_-+L_{\text{sep}}+L_+} = \frac{I}{A}$, $\left.\frac{\partial\phi_s}{\partial x}\right\|_{x=L_-} = \left.\frac{\partial\phi_s}{\partial x}\right\|_{x=L_-+L_{\text{sep}}} = 0$ |
| Species | | | |
| Electrolyte phase | $\frac{\partial(\varepsilon_e c_e)}{\partial t} = \frac{\partial}{\partial x}\left(D_e^{\text{eff}}\frac{\partial}{\partial x}c_e\right) + \frac{1-t_+^0}{F}j^{\text{Li}}$ | (3) | $\left.\frac{\partial c_e}{\partial x}\right\|_{x=0} = \left.\frac{\partial c_e}{\partial x}\right\|_{x=L} = 0$ |
| Solid phase | $\frac{\partial c_s}{\partial t} = \frac{D_s}{r^2}\frac{\partial}{\partial r}\left(r^2\frac{\partial c_s}{\partial r}\right)$ | (4) | $\left.\frac{\partial c_s}{\partial r}\right\|_{r=0} = 0$, $D_s\left.\frac{\partial c_s}{\partial r}\right\|_{r=R_s} = -\frac{j^{\text{Li}}}{a_s F}$ |

solid phase concentration at the particle surface, $c_{s,e} = c_s|_{r=R_s}$, to evaluate local equilibrium potential, $U$, and exchange current density, $i_0$. Authors have used various approaches in their treatment of Eq. (4), including an analytical solution implemented as a Duhamel superposition integral [11], a parabolic concentration profile model [19], and a sixth-order polynomial profile model [20]. In the present work we approximate Eq. (4) using the finite element method as described in Appendix A. Spatial discretization with five linear elements unevenly spaced along the particle radius provides sufficient resolution of $c_{s,e}(t)$ as a function of $j^{Li}(t)$ at both short and long times. The various approaches to solid-state diffusion modeling are contrasted and discussed in Section 4.

For numerical solution, the 1D macroscopic domain is discretized into approximately 70 control volumes in the $x$-direction. The solid diffusion submodel (Appendix A) is separately applied within each control volume of the negative and positive electrodes. The four governing equations (Table 1) are solved simultaneously for field variables $c_e$, $c_{s,e}$, $\phi_e$, and $\phi_s$. Current is used as the model input and boundary conditions are therefore applied galvanostatically. Cell terminal voltage is determined by the equation:

$$V = \phi_s|_{x=L} - \phi_s|_{x=0} - \frac{R_f}{A} I, \tag{7}$$

where $R_f$ represents a contact resistance between current collectors and electrodes.

## 3. Model parameterization

Low-rate static discharge/charge, hybrid pulse power characterization (HPPC), and transient driving cycle data were provided by the DOE FreedomCAR program for a 276 V nominal HEV battery pack consisting of 72 serially connected cells. Data was collected according to Freedom CAR test procedures [4]. For the purpose of HEV systems integration modeling [21], we were tasked to build a mathematical model of single cell of that pack. We make no attempt to account for cell-to-cell variability and present all data on a single cell basis by dividing measured pack voltage by 72. Due to the proprietary nature of the prototype FreedomCAR battery we were unable to disassemble cells to measure geometry, composition, etc., and thus adopt values from the literature and adjust them as necessary to fit the data. By expressing capacity of the negative and positive electrodes as

$$Q_- = \varepsilon_{s-}(L_- A)(c_{s,\max-})(\Delta x)F,$$
$$Q_+ = \varepsilon_{s+}(L_+ A)(c_{s,\max+})(\Delta y)F, \tag{8}$$

low-rate capacity data provides a rough gauge of electrode volume and stoichiometry cycling range, assuming electrode composition and electrode mass ratio values from Ref. [2]. This mass ratio is later shown to result in a well-balanced cell at both high and low rates. Discharge capacity at the 1 C (6 A) rate was measured to be 7.2 Ah and we define stoichiometry reference points for 0% and 100% SOC (listed in Table 2) on a 7.2 Ah basis.

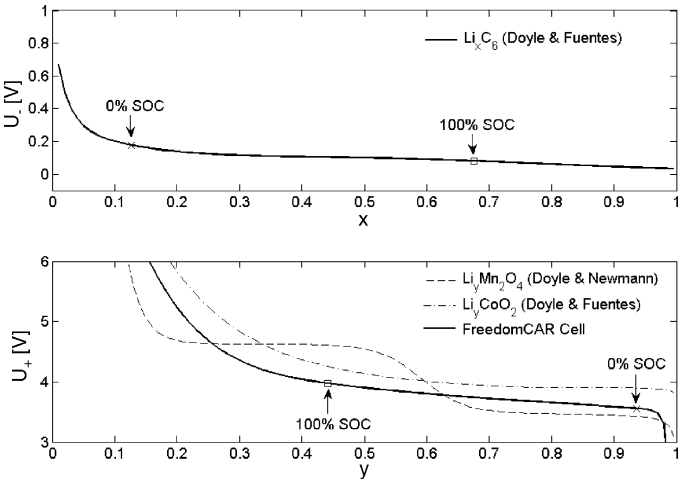


Fig. 2. Empirical open-circuit potential relationships for negative and positive electrodes.

The negative electrode active material almost certainly consists of graphite ($Li_xC_6$) given its widespread use in reversible lithium ion cells. Shown in Fig. 2, we use the empirical correlation for $Li_xC_6$ open-circuit potential, $U_-$, from Ref. [2]. The positive electrode active material could consist of $Li_yMn_2O_4$, $Li_yCoO_2$, $Li_yNiO_2$, or some combination of metal oxides. Listed in Table 2, we fit our own correlation for $U_+$ by subtracting $U_-$ from the cell's measured open-circuit voltage.

Fig. 3 compares the model using parameters listed in Table 2 to 1 C (6 A) constant current discharge and charge data. This low-rate data set is relatively easy to fit as it deviates little from open-circuit voltage.

In contrast, the voltage perturbation of the transient HPPC data set is more difficult to fit. The HPPC test procedure, defined in [4], consists of a 30 A discharge for 18 s, open-circuit relaxation for 32 s, 22.5 A charge for 10 s, followed by open-circuit relaxation as shown in the top window of Fig. 4. The onset of constant current discharge and charge portions of the HPPC profile are accompanied by brief (0.1 s) high-rate pulses to

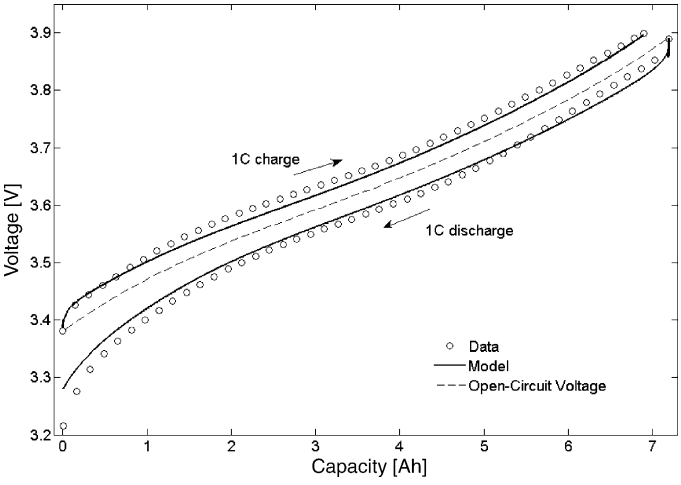


Fig. 3. Model validation versus constant current charge/discharge data at 1 C (6 A) rate.

Table 2
FreedomCAR cell model parameters

| Parameter | Negative electrode | Separator | Positive electrode |
|---|---|---|---|
| Design specifications (geometry and volume fractions) | | | |
| Thickness, $\delta$ ($\times 10^{-4}$ cm) | 50 | 25.4 | 36.4 |
| Particle radius, $R_s$ ($\times 10^{-4}$ cm) | 1 | | 1 |
| Active material volume fraction, $\varepsilon_s$ | 0.580 | | 0.500 |
| Polymer phase volume fraction, $\varepsilon_p$ | 0.048 | 0.5 | 0.110 |
| Conductive filler volume fraction, $\varepsilon_f$ | 0.040 | | 0.06 |
| Porosity (electrolyte phase volume fraction), $\varepsilon_e$ | 0.332 | 0.5 | 0.330 |
| Solid and electrolyte phase $Li^+$ concentration | | | |
| Maximum solid phase concentration $c_{s,max}$ ($\times 10^{-3}$ mol cm$^{-3}$) | 16.1 | | 23.9 |
| Stoichiometry at 0% SOC, $x_{0\%}$, $y_{0\%}$ | 0.126 | | 0.936 |
| Stoichiometry at 100% SOC, $x_{100\%}$, $y_{100\%}$ | 0.676 | | 0.442 |
| Average electrolyte concentration, $c_e$ ($\times 10^{-3}$ mol cm$^{-3}$) | 1.2 | 1.2 | 1.2 |
| Kinetic and transport properties | | | |
| Exchange current density, $i_0$ ($\times 10^{-3}$ A cm$^{-2}$) | 3.6 | | 2.6 |
| Charge-transfer coefficients, $\alpha_a$, $\alpha_c$ | 0.5, 0.5 | | 0.5, 0.5 |
| SEI layer film resistance, $R_{SEI}$ ($\Omega$ cm$^2$) | 0 | | 0 |
| Solid phase Li diffusion coefficient, $D_s$ ($\times 10^{-12}$ cm$^2$ s$^{-1}$) | 2.0 | | 3.7 |
| Solid phase conductivity, $\sigma$ (S cm$^{-1}$) | 1.0 | | 0.1 |
| Electrolyte phase $Li^+$ diffusion coefficient, $D_e$ ($\times 10^{-6}$ cm$^2$ s$^{-1}$) | 2.6 | 2.6 | 2.6 |
| Bruggeman porosity exponent, $p$ | 1.5 | 1.5 | 1.5 |
| Electrolyte phase ionic conductivity, $\kappa$ (S cm$^{-1}$) | $\kappa = 0.0158c_e \exp(0.85c_e^{1.4})$ | $\kappa = 0.0158c_e \exp(0.85c_e^{1.4})$ | $\kappa = 0.0158c_e \exp(0.85c_e^{1.4})$ |
| Electrolyte activity coefficient, $f_\pm$ | 1.0 | 1.0 | 1.0 |
| $Li^+$ transference number, $t_+^0$ | 0.363 | 0.363 | 0.363 |

| Parameter | Value |
|---|---|
| Equilibrium potential | |
| Negative electrode, $U_-$ (V) | $U_-(x) = 8.00229 + 5.0647x - 12.578x^{1/2} - 8.6322 \times 10^{-4}x^{-1} + 2.1765 \times 10^{-5}x^{3/2} - 0.46016\exp[15.0(0.06 - x)] - 0.55364\exp[-2.4326(x - 0.92)]$ |
| Positive electrode, $U_+$ (V) | $U_+(y) = 85.681y^6 - 357.70y^5 + 613.89y^4 - 555.65y^3 + 281.06y^2 - 76.648y - 0.30987\exp(5.657y^{115.0}) + 13.1983$ |
| Plate area-specific parameters | |
| Electrode plate area, $A$ (cm$^2$) | 10452 |
| Current collector contact resistance, $R_f$ ($\Omega$ cm$^2$) | 20 |

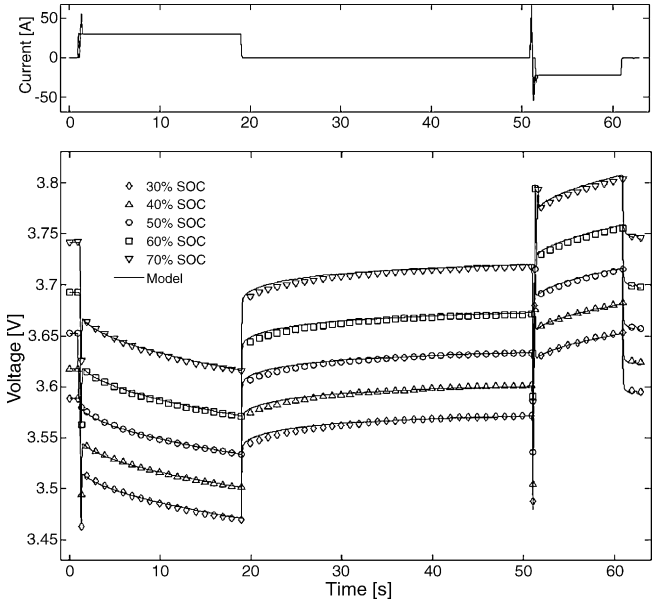


Fig. 4. Model validation versus HPPC test data. SOC labeled on 6 Ah-basis per FreedomCAR test procedures. SOC initial conditions used in 7.2 Ah-basis model are 41.7%, 50.0%, 58.3%, 66.6%, and 75.0%.

estimate high-frequency resistance. Unable to decouple values of SEI layer resistance from contact film resistance (or cell-to-cell interconnect resistance for that matter), we fit ohmic perturbation using a contact film resistance of $R_f = 20\ \Omega\ cm^2$.

Neglecting double-layer capacitance for reasons noted earlier, the only transient phenomena accounted for in the governing equations (here and in other work [14]) are electrolyte diffusion and solid diffusion. A parametric study showed that while it was possible to match the observed voltage drop at the end of the HPPC 30 A discharge by lowering $D_e$ several orders of magnitude from a baseline value of $2.6 \times 10^{-6}$ cm$^2$ s$^{-1}$ [2], the voltage drop at short times was too severe. Significant decrease in $D_e$ also caused predicted voltage to diverge from the measured voltage over time due to severe electrolyte concentration gradients. While recent $LiPF_6$-based electrolyte property measurements [22] show diffusion coefficient, $D_e$, and activity coefficient, $f_\pm$, both exhibiting moderate concentration dependency, it is beyond the scope of this work to consider anything beyond the first approximation of constant $D_e$ and unity $f_\pm$.

In investigating solid-state diffusion transient effects, we note that measured voltage response only allows observation

of characteristic time $t = R_s^2/D_s$ and will not provide $R_s$ and $D_s$ independently. SEM images, such as that shown by Dees et al. [23] (their Fig. 1) of a $LiNi_{0.8}Co_{0.15}Al_{0.05}O_2$ composite electrode, often show bulk or "secondary" active material particles (with radii ~5 μm) having finer "primary" particles (with radii ~0.5 μm) attached to the surface. Dees achieved good description of $LiNi_{0.8}Co_{0.15}Al_{0.05}O_2$ impedance data in the 0.01–1 Hz frequency range using a characteristic diffusion length of 1.0 μm. As active material composition and structure are unknown for the present cell, we adopt this value as the particle radius in both electrodes.

Though $Li_xC_6$ is often reported to have more sluggish diffusion than common positive electrode active materials, a parametric study on $D_{s-}$ using the transient solid diffusion model found no value capable of describing both the ~0.047 V drop in cell voltage from 2 to 20 s of the HPPC test as well as the slow voltage relaxation upon open-circuit at 20 s. Assuming for the moment that the ~0.047 V drop is caused solely by solid diffusion limitations in the negative electrode, we estimate that surface concentration $c_{s,e-}$ would need to fall from its initial value by $4.3 \times 10^{-4}$ mol cm$^{-3}$ (a substantial amount) to cause the observed 0.047 V change in $U_-$. Wang and Srinivasan [24] give an empirical formula for the evolution of a concentration gradient within a spherical particle subjected to constant surface flux as

$$c_{s,e}(t) - c_{s,avg}(t) = j^{Li}\frac{-R_s}{5a_s F D_s}\left[1 - \exp\left(-\frac{20}{3}\frac{\sqrt{D_s t}}{R_s}\right)\right]. \quad (9)$$

At steady state (where the exponential term goes to zero) and with the assumption of uniform reaction current density, $j_-^{Li} = I/AL_-$, we manipulate Eq. (9) to obtain a rough estimate of the negative electrode diffusion coefficient:

$$D_{s-} = \frac{R_s}{5Fa_s\Delta c_{s-}}\frac{I}{AL_-} \quad (10)$$

of $1.6 \times 10^{-12}$ cm$^2$ s$^{-1}$. A corresponding characteristic time whereby the operand of the exponential term in Eq. (9) equals unity is 140 s. Our conclusion is that, while a negative electrode solid diffusion coefficient of $D_{s-} = 1.6 \times 10^{-12}$ cm$^2$ s$^{-1}$ might cause the cell voltage to drop ~0.047 V, that voltage drop would take much longer to develop than what we observe in the data. Repeating calculations for concentration gradient magnitude and characteristic time under a variety of conditions revealed that the observed transient behavior might be described by solid-state diffusion in the negative electrode if the slope $\partial U_-/\partial c_{s-}$ were roughly eight times steeper. This is indeed the case in the positive electrode, where at 50% SOC the open-circuit potential function has almost seven times greater slope with respect to concentration than the negative electrode. Chosen via parametric study, final values of $D_{s-}$ ($2.0 \times 10^{-12}$ cm$^2$ s$^{-1}$) and $D_{s+}$ ($3.7 \times 10^{-12}$ cm$^2$ s$^{-1}$) represent HPPC voltage dynamics in Fig. 4 quite well, although we note they are dependent upon our choice of particle radius. Were we to chose particle radii of 5 μm rather than 1 μm, our diffusion coefficient would be 25 times higher to maintain characteristic time $t = R_s^2/D_s$ and match the voltage dynamics of the HPPC test.

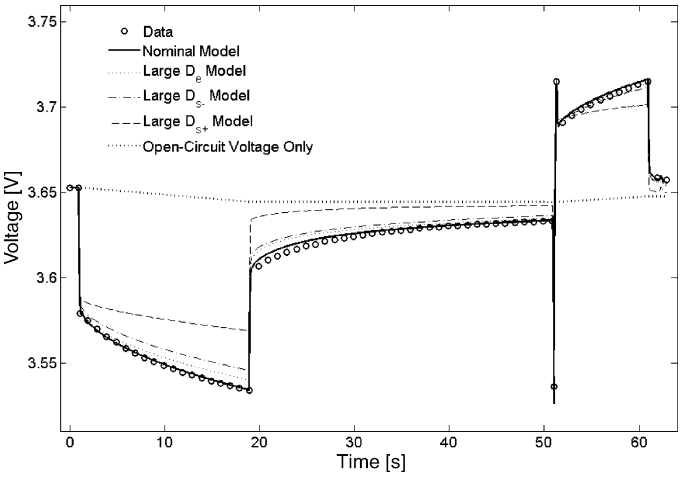


Fig. 5. Nominal model compared to models where limitations of electrolyte phase, negative electrode solid phase, and positive electrode solid phase diffusion have been individually (not sequentially) removed.

Fig. 5 quantifies voltage polarization resulting from diffusional transport by individually raising each diffusion coefficient by five or more orders of magnitude such that it no longer affects cell voltage response. Despite comparable values of $D_{s-}$ and $D_{s+}$, the positive electrode polarizes transient voltage response more significantly due to its stronger open-circuit potential coupling.

Fig. 6 compares model voltage prediction to data taken on the FreedomCAR battery whereby an ABC-150 battery tester was used to mimic a power profile recorded from a Toyota Prius HEV on a federal urban (FUDS) driving cycle. Only the first 150 s are shown, though results are representative of the entire test.

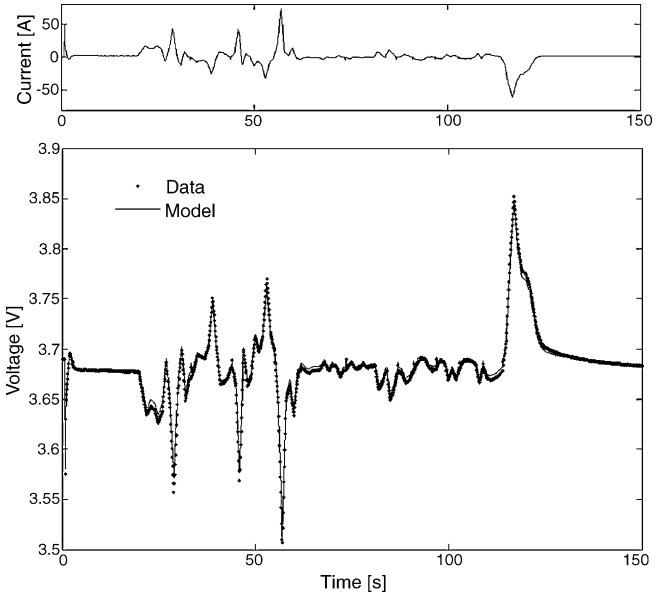


Fig. 6. Model validation versus transient FUDS cycle HEV data. Power profile of data mimics that recorded from a Toyota Prius (passenger car) HEV run on a chassis dynamometer.

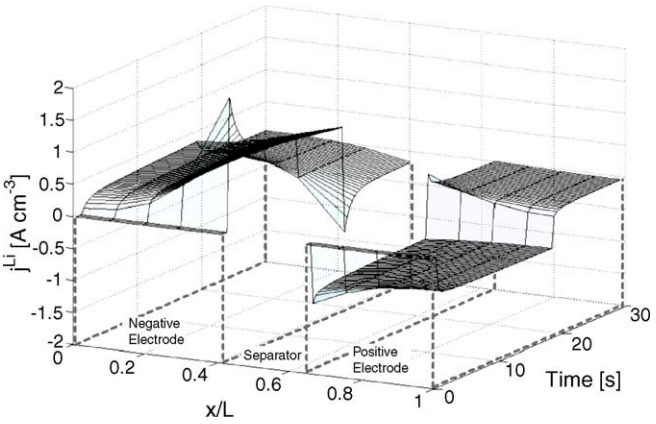


Fig. 7. Distribution of reaction current across cell for first 30 s of HPPC test at 58.3% SOC.

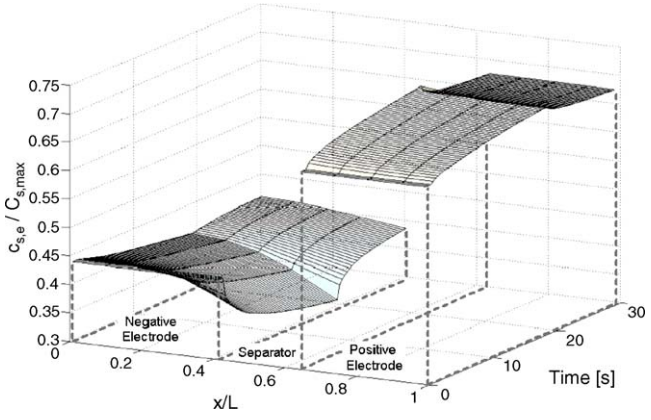


Fig. 8. Distribution of active material surface concentration across cell for first 30 s of HPPC test at 58.3% SOC.

## 4. Results and discussion

### 4.1. Reaction dynamics

Despite aforementioned uncertainties in cell design and choice of model parameters, the model is still useful in elucidating pulse discharge and charge dynamics resulting from solid phase transport limitations. As a basis for the subsequent discussion we use simulation results from the first 30 s of the 58.3% SOC HPPC case (whose voltage response is denoted with circles in Fig. 4).

Approximately one second into the test, a 30 A discharge current is applied resulting in the step change in local reaction current, $j^{Li}$, shown in Fig. 7. At the onset of the step change, solid phase surface concentrations are uniform and the initial distribution of reaction across each electrode is governed by relative magnitudes of exchange current density, electrolyte phase conductivity, and solid phase conductivity. The solid phase is a much better conductor than the electrolyte phase and the reaction is distributed such that $Li^+$ ions favor a path of least resistance, traveling the shortest distance possible in the electrolyte phase. Negative electrode reaction is less evenly distributed than positive electrode reaction predominantly due to the greater solid phase conductivity of the negative electrode ($\sigma_- = 1.0\,S\,cm^{-1}$ versus $\sigma_+ = 0.1\,S\,cm^{-1}$).

As a consequence of the initial peak in reaction current at the separator interface, Li surface concentration changes most rapidly at that location in each electrode, as shown in Fig. 8. The effect is more pronounced in the negative electrode where the larger initial peak in current density quickly causes a gradient in active material surface concentration, $\partial c_{s,e}/\partial x$, to build across that electrode. Local equilibrium potential, $U_-$, falls most rapidly at the negative electrode/separator interface, penalizing further reaction at that location and driving the redistribution of reaction shown in Fig. 7. As discharge continues, progressively less reaction occurs at the separator interface and more reaction occurs at the current collector interface.

Positive electrode reaction current exhibits similar redistribution, though less significant than in the negative electrode for two reasons. First, at the onset of the 30 A discharge, initial reaction distribution is already more uniform in the positive electrode. Second, and more significant, the positive electrode open-circuit potential function is almost seven times more sensitive to changes in concentration than the negative electrode function at 58.3% SOC. Small changes in positive electrode active material surface concentration significantly penalize reaction, and for this reason, redistribution of reaction due to solid diffusion limitations occurs much quicker in that electrode.

Redistribution of Li also occurs upon cell relaxation at the end of the 18 s-long 30 A discharge. Fig. 7 shows a second step change in transfer current density around 19 s, appearing qualitatively as the mirror image of the step change at 1 s when the galvanostatic load was first applied. At locations near the separator, a recharging process begins while at locations near the current collector, discharge continues even after the load is removed. The process is driven by the gradient in local equilibrium potential, $\partial U/\partial x$ (directly related to the solid phase surface concentration gradient, $\partial c_{s,e}/\partial x$) and continues until surface concentrations, $c_{s,e}$, are once again evenly distributed. During this redistribution process the net balance of reaction across each electrode is zero.

Relaxation reaction redistribution is less significant in the positive electrode, where only a minimal solid phase surface concentration gradient, $\partial c_{s,e}/\partial x$, arose during the 30 A discharge. The process lasts on the order of 10 s, compared to several minutes for the negative electrode. In both electrodes, solid phase bulk concentrations rise and fall at roughly the same rate as surface concentrations throughout the redistribution process, indicating that the time scale of reaction redistribution is much faster than solid phase diffusion. Localized concentration gradients within individual solid particles (from bulk to surface), $\partial c_s/\partial r$, relax so slowly that the 63 s long pulse power test amounts to little more than a transient discharge and charge on the surface of the active material particles with inner bulk regions unaffected.

### 4.2. Rate capability

Fig. 9 presents model-predicted constant current discharge capability from 50% SOC. Shown in the bottom window of

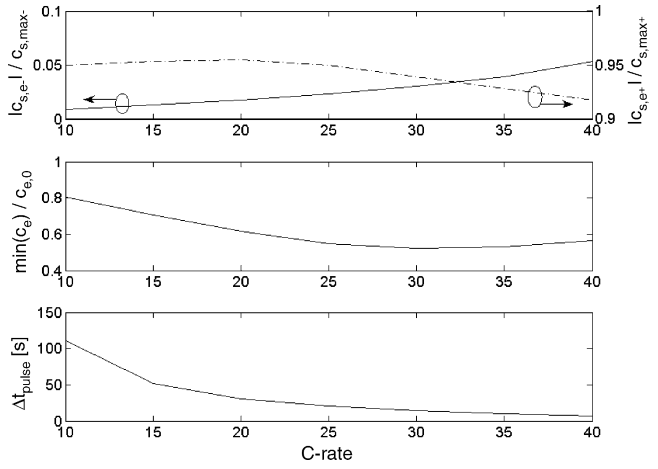


Fig. 9. Solid phase surface concentration (top), minimum electrolyte concentration (middle), and time (bottom) at end of galvanostatic discharge for rates from 10 to 40 C.

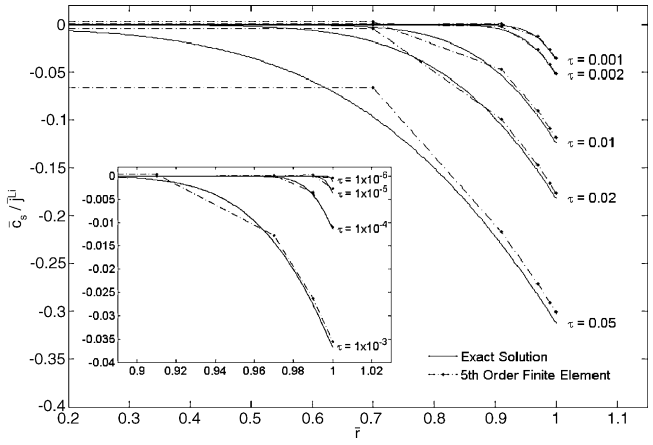


Fig. 10. Dimensionless distribution of concentration within an active material particle at various times during galvanostatic (dis)charge.

Fig. 9, a 40 C rate current (240 A) can be sustained for just over 6 s before voltage decays to the 2.7 V minimum. The top window of Fig. 9 shows active material surface concentration in the negative (left axis) and positive (right axis) electrodes at the end of discharge across the range of discharge rates. Electrode-averaged rather than local values of surface concentration are presented to simplify the discussion. The electrodes are fairly well balanced, indicated by end of discharge surface concentrations near depletion and saturation in the negative and positive electrodes, respectively. End of discharge voltage is predominantly negative electrode-limited as stoichiometries of $x = c_{s,e}/c_{s,max-} < 0.05$ causes a rapid rise in $U_-$. Surface active material utilization decreases slightly with increasing C-rate due to increased ohmic voltage drop.

In the present model, electrolyte $Li^+$ transport is sufficiently fast that electrolyte depletion does not play a limiting role at any discharge rate from 50% SOC. In the worst case of 30 C, the minimum value of local electrolyte concentration, occurring at the positive electrode/current collector interface, is around 50% of average concentration, $c_{e,0}$. For rates less than 30 C, the reduced current level results in lesser electrolyte concentration gradients, while for rates greater than 30 C, the shorter duration of discharge time results in a smaller concentration gradient at end of discharge. If we induce sluggish diffusion by reducing $D_e$ (a similar effect may be induced in cell design by reducing porosity), electrolyte concentration in the positive electrode comes closer to depletion with the worst case minimum value of $c_e$ occurring at lesser current rates. Lowering $D_e$ by one order of magnitude for example, results in a battery limited in the 10–20 C range by electrolyte phase transport, with higher and lower current rates still controlled by solid phase transport.

### 4.3. Solid-state diffusion limited current

Under solid phase transport limitations, simple relationships may be derived to predict maximum current available for a given pulse time. Substituting dimensionless variables:

$$\bar{r} = \frac{r}{R_s}, \qquad \tau = \frac{D_s t}{R_s^2}, \qquad \bar{c}_s(\bar{r},\tau) = \frac{c_s(\bar{r},\tau) - c_{s,0}}{c_{s,max}},$$

$$\bar{j}^{Li} = \frac{j^{Li} R_s}{D_s a_s F c_{s,max}} \tag{11}$$

into Eq. (4) yields the dimensionless governing equation:

$$\frac{\partial \bar{c}_s}{\partial \tau} = \frac{1}{\bar{r}^2}\frac{\partial}{\partial \bar{r}}\left(\bar{r}^2 \frac{\partial \bar{c}_s}{\partial \bar{r}}\right) \tag{12}$$

with initial condition $\bar{c}_s(\bar{r}, \tau = 0) = 0\,\forall\,\bar{r}$ and boundary conditions:

$$\left.\frac{\partial \bar{c}_s}{\partial \bar{r}}\right|_{\bar{r}=0} = 0, \qquad \left.\frac{\partial \bar{c}_s}{\partial \bar{r}}\right|_{\bar{r}=1} = \bar{j}^{Li}. \tag{13}$$

The solution given by Carslaw and Jaeger [25] is

$$\bar{c}_s(\bar{r},\tau) = -\bar{j}^{Li}\left[3\tau + \frac{1}{10}(5\bar{r}^2 - 3) - \frac{2}{\bar{r}}\sum_{n=1}^{\infty}\frac{\sin(\lambda_n \bar{r})\exp(-\lambda_n^2\tau)}{\lambda_n^2 \sin(\lambda_n)}\right], \tag{14}$$

where the eigenvalues are roots of $\lambda_n = \tan(\lambda_n)$. Fig. 10 shows distribution of Li concentration along the radius of an active material particle during galvanostatic discharge or charge for dimensionless times ranging from $\tau = 10^{-6}$ to $10^{-1}$ which, for reference, correspond to current pulses lasting 0.05–500 s using negative electrode parameters from Table 2.

Surface concentration and depth of penetration into the active material, both of practical interest for HEV pulse-type operation, can be obtained from Eq. (14). Surface concentration, shown for the present model to cause end of discharge as the negative electrode nears depletion, is calculated by evaluating Eq. (14) at $\bar{r} = 1$. Penetration depth, $\delta$, providing a measure of active material accessible for short duration pulse events, is calculated by finding the point along the radius where the concentration profile is more or less equal to the initial condition. A 99% penetration

Table 3
Empirical formulae fit to solid-state diffusion PDE exact solution, Eq. (14)

| | | 1% error bounds |
|---|---|---|
| Dimensionless surface concentration | | |
| $\frac{\bar{c}_{s,e}}{\bar{j}^{Li}} = -1.139\sqrt{\tau}$ | (16) | $0<\tau<1\times10^{-4}$ |
| $\frac{\bar{c}_{s,e}}{\bar{j}^{Li}} = -1.122\sqrt{\tau} - 1.25\tau$ | (17) | $0<\tau<8\times10^{-2}$ |
| Dimensionless 99% penetration depth | | |
| $\bar{\delta} = 3.24\sqrt{\tau}$ | (18) | $0<\tau<1\times10^{-3}$ |
| $\bar{\delta} = 3.23\sqrt{\tau} + 1.89\tau$ | (19) | $0<\tau<2\times10^{-2}$ |

depth, $\delta = R_s - r$, is defined using the location $r$ resulting in a root of the formula:

$$\frac{\bar{c}_s(\bar{r},\tau)}{\bar{c}_s(1,\tau)} = 1 - a \tag{15}$$

with $a = 0.99$. Expressed as a fraction of total radius, dimensionless penetration depth, $\bar{\delta} = \delta/R_s$, is a function of dimensionless time only.

Empirical expressions for dimensionless surface concentration, $\bar{c}_{s,e}$, and dimensionless penetration depth, $\bar{\delta}$, are fit to the results of Eq. (14) and presented in Table 3. Functions of the form $f(\tau) = C\sqrt{\tau}$ provide good resolution at short times of $\tau < 10^{-3}$, corresponding in our model to pulses lasting fewer than ~5 s. Resolution may be extended one to two orders of magnitude in $\tau$ by using functions of the form $f(\tau) = C\sqrt{\tau} + D\tau$. The latter functions are plotted versus the exact solution (14) in Fig. 11.

Eq. (17) in Table 3 may be used in lieu of the present electrochemical model to predict negative electrode surface concentrations for pulses shorter than 400 s, or, conversely, to predict limiting currents at rates greater than ~9 C caused by depleted active material surface concentration at end of discharge. By combining Eqs. (11) and (17) under the assumption of uniform current density, $j_-^{Li} = I/AL_-$, we obtain an empirical relationship for surface concentration as a function of current and time:

$$\frac{c_{s,e}(t)}{c_{s,max-}} = \frac{c_{s,0}}{c_{s,max-}} - I\frac{R_{s-}}{L_- A D_{s-} a_{s-} F c_{s,max-}} \times \left[1.122\frac{\sqrt{D_{s-}t}}{R_{s-}} + 1.25\frac{D_{s-}t}{R_{s-}^2}\right] \tag{20}$$

valid for $t < 0.08 D_s/R_s^2$. Alternatively, given initial stoichiometry, $x_0$, and surface stoichiometry at end of discharge, $x_{s,e\,final}$, the maximum current available for a pulse discharge lasting $t$ seconds will be

$$I_{max} = (x_0 - x_{s,e\,final})\left(\frac{L_- A a_{s-} F c_{s,max-}}{\frac{1.122}{\sqrt{D_{s-}}}\sqrt{t} + \frac{1.25}{R_{s-}}t}\right). \tag{21}$$

While the theoretical maximum current will be obtained under the condition $x_{s,e\,final} = 0$, i.e. complete surface depletion, Fig. 9 showed the present model to exhibit an end of discharge surface stoichiometry around 0.03, with some rate dependency. Under uniform initial conditions, the initial stoichiometry, $x_0$, is simply a function of SOC. For a recently charged or discharged battery with nonuniform initial concentration, a better prediction of maximum pulse current may be obtained by replacing $x_0$ in Eq. (21) with a stoichiometry averaged across the penetration depth or "pulse-accessible" region [26].

### 4.4. Suitability of solid-state diffusion approximations for cell modeling

Introduced in Section 2 and detailed in Appendix A, the present work utilizes a fifth-order finite element approximation for solid-state diffusion (4) and incorporates that submodel into the 1D electrochemical model as a finite difference equation, that is, local values of $c_{s,e}$ are calculated using values of $c_{s,e}$ and $j^{Li}$ from the previous five time steps:

$$c_{s,e}^{[k]} = f([c_{s,e}^{[k-1]}, \ldots, c_{s,e}^{[k-5]}], [j^{Li[k]}, \ldots, j^{Li[k-5]}]). \tag{22}$$

Here we compare the finite element submodel to the analytical solution employed by Doyle et al. [11] and the polynomial profile model of Wang et al. [19]. Comparisons are made in the frequency domain in order to remove the influence of a particular type of input (pulse current, current step, constant current, etc.) by taking the Laplace transform of each time domain model, expressing the input/output relationship as a transfer function in the Laplace variable $s$, and substituting $s = j\omega$ to calculate the complex impedance at frequency $\omega$. A capitalized variable denotes that variable's Laplace transform, that is, $C_{s,e}(s) = L\{c_{s,e}(t)\}$, and an overbar denotes a dimensionless variable. Define

$$\bar{C}_{s,e}(s) = \frac{C_{s,e}(s) - c_{s,0}}{c_{s,max}}, \qquad \bar{J}^{Li}(s) = J^{Li}(s)\frac{R_s}{a_s F D_s c_{s,max}},$$
$$\bar{\omega} = \omega\frac{R_s^2}{D_s}. \tag{23}$$

In the Laplace domain, a compact analytical solution to Eq. (4) is readily available. The exact transfer function expressing

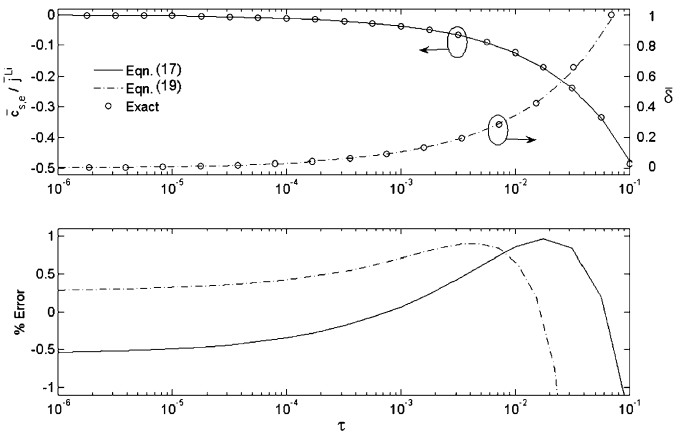


Fig. 11. Dimensionless active material surface concentration and penetration depth versus time (top). Percent error in empirical correlations of the form $f(\tau) = C\sqrt{\tau} + D\tau$ (bottom).

dimensionless surface concentration versus dimensionless reaction current given by Jacobsen and West [28] is

$$\frac{\bar{C}_{s,e}(s)}{\bar{J}^{Li}(s)} = \frac{\tanh(\psi)}{\tanh(\psi) - \psi}, \tag{24}$$

where $\psi = R_s\sqrt{s/D_s}$.

Doyle et al. [11] provide two analytical series solutions in the time domain, one for short times and one for long times. In Appendix B, we manipulate Doyle's formulae to arrive at the short time transfer function:

$$\frac{\bar{C}_{s,e}(s)}{\bar{J}^{Li}(s)} = \left[1 - \psi + 2\psi\sum_{n=1}^{\infty}\exp(-2n\psi)\right]^{-1} \tag{25}$$

and the long time transfer function:

$$\frac{\bar{C}_{s,e}(s)}{\bar{J}^{Li}(s)} = \left[-2\sum_{n=1}^{\infty}\frac{\psi^2}{\psi^2 + \frac{(n\pi R_s)^2}{D_s}}\right]^{-1}. \tag{26}$$

The frequency response (magnitude and phase angle) of truncated versions of the short and long time transfer functions are compared to the exact transfer function (24) in Fig. 12, showing the short time solution to provide good agreement at high frequencies and the long time solution at low frequencies. Note that the short time transfer function does not change much beyond the first term of the series. A good strategy to piece together Doyle's two solutions is to use one term of the short time solution for $\tau = D_s t/R_s^2 \leq 0.1$ (corresponding to $\bar{\omega} = 6 \times 10^1$ in Fig. 12) and around 100 terms of the long time solution for $\tau > 0.1$.

Reaction current appears in Eq. (4) as a time dependent boundary condition which Doyle accommodates using a Duhamel superposition integral. Numerical solution of this convolution-type integral requires that a time history of all previous step changes in surface concentration be held in memory and called upon at each time step to reevaluate the integral. So while the analytical solution is inarguably the most accurate approach, it can be expensive in terms of memory and computational requirements, particularly in situations requiring a small

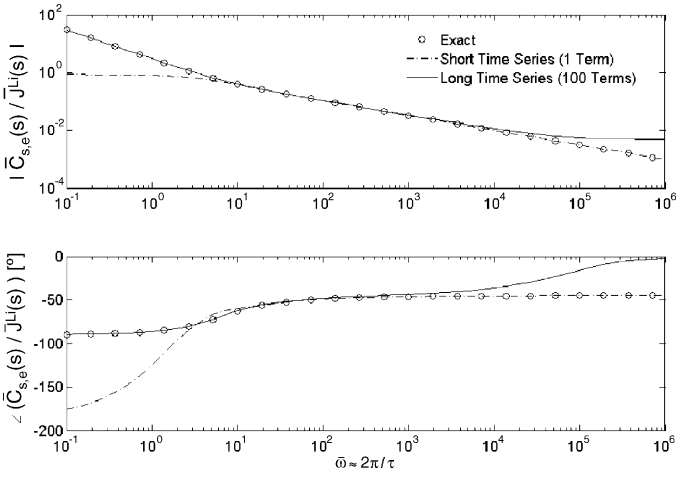


Fig. 12. Frequency response of short and long time analytical solutions used in Ref. [11] for solid-state diffusion in spherical particles, compared to exact frequency response from Ref. [28].

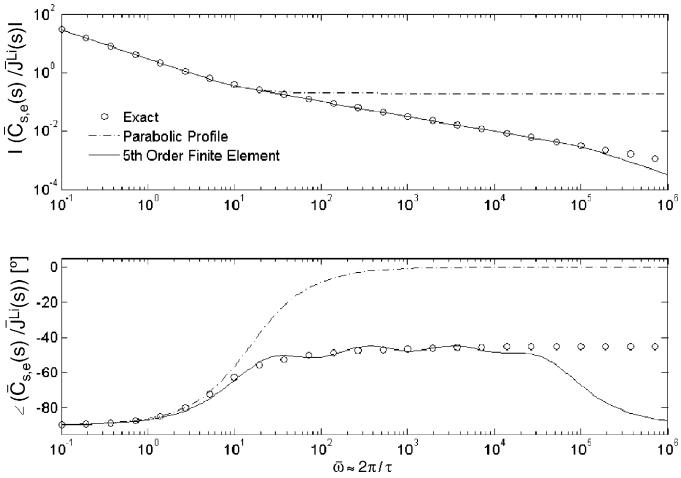


Fig. 13. Frequency response of parabolic profile solid-state diffusion submodel from Ref. [19] and fifth-order finite element solid-state diffusion submodel (used in this work), compared to exact frequency response from Ref. [28].

time step but long simulation time (driving cycle simulations, for instance) or in situations requiring a large grid mesh (2D or 3D simulations incorporating realistic cell geometry, for instance).

Approximate solutions to Eq. (4) are appropriate so long as they capture solid-state diffusion dynamics sufficiently fast for a particular investigation. Wang et al. [19] assume the concentration profile within the spherical particle is described by a parabolic profile $c_s(r, t) = A(t) + B(t)r^2$, and thus formulate a solid-state diffusion submodel which correctly captures bulk dynamics and steady state concentration gradient, but otherwise neglects diffusion dynamics. Derived in Appendix C, the transfer function of the parabolic profile, or steady state diffusion, model is

$$\frac{\bar{C}_{s,e}(s)}{\bar{J}^{Li}(s)} = \frac{3}{\psi^2} + \frac{1}{5}. \tag{27}$$

Shown in Fig. 13 versus the exact transfer function (24), the parabolic profile model is valid for low frequencies, $\bar{\omega} < 10$, or long times, $\tau = D_s t/R_s^2 > 0.6$. Substituting values from the present model's negative electrode ($D_{s-} = 2.0 \times 10^{-12}$ cm$^2$ s$^{-1}$, $R_{s-} = 1.0 \times 10^{-4}$ cm), the parabolic profile model would correctly predict surface concentration only at times longer than 3000 s. For electrochemical cells with sluggish solid-state diffusion, the parabolic profile model will correctly capture low-rate end of discharge behavior, but is generally inappropriate in the modeling of high rate (>2 C) or pulse type applications [27].

We find spatial discretization of Eq. (4) yields low-order solid-state diffusion models with more accurate short time prediction compared to polynomial profile models [20]. Recasting the fifth-order finite element model from Appendix A in nondimensional form:

$$\frac{\bar{C}_{s,e}(s)}{\bar{J}^{Li}(s)} = a_s F\frac{D_s}{R_s}\left[\frac{b_1 s^5 + b_2 s^4 + b_3 s^3 + b_4 s^2 + b_5 s + b_6}{a_1 s^5 + a_2 s^4 + a_3 s^3 + a_4 s^2 + a_5 s + a_6}\right]. \tag{28}$$

Fig. 13 shows the present model to provide good approximation of the exact transfer function (26) for $\bar{\omega} < 10^5$, and thus be valid

for dimensionless times $\tau > 6 \times 10^{-5}$ (or $t > 0.3$ s for the present model's negative electrode). Regardless of what solution technique is employed for solid-state diffusion in an electrochemical cell model, if the objective is to match high-rate (~40 C) pulse behavior and predict transport limitations on a short (~5 s) time scale, that technique must be valid at very short times.

## 5. Conclusions

A fifth-order finite element model for transient solid-state diffusion is incorporated into a previously developed 1D electrochemical model and used to describe low-rate constant current, hybrid pulse power characterization, and transient driving cycle data sets from a lithium ion HEV battery. HEV battery models in particular must accurately resolve active material surface concentration at very short dimensionless times. Requirements for the present model are $t = D_s t/R_s^2 \approx 10^{-3}$ to predict 40 C rate capability and $\tau \approx 2 \times 10^{-5}$ to match current/voltage dynamics at 10 Hz.

Dependent on cell design and operating condition, end of pulse discharge may be caused by negative electrode solid phase Li depletion, positive electrode solid phase Li saturation, or electrolyte phase Li depletion. Simple expressions developed here for solid-state diffusion-limited current, applicable in either electrode, may aid in the interpretation of high-rate experimental data. While the present work helps to extend existing literature into the dynamic operating regime of HEV batteries, future work remains to fully characterize an HEV battery in the laboratory and develop a fundamental model capable of matching current/voltage data at very high rates.

## Acknowledgements

This work was funded by the U.S. Department of Energy, Office of FreedomCAR and Vehicle Technologies through Argonne National Laboratory (Program Manager: Lee Slezak). We thank Aymeric Rousseau and Argonne National Laboratory for providing battery experimental data as well as Dr. Marc Doyle and Dr. Venkat Srinivasan for helpful discussions.

## Appendix A

### A.1. Solid-state diffusion finite element model

The transient phenomenon of solid-state Li diffusion is incorporated into the previously developed macroscopic model of Gu and Wang [3]. While the governing Eq. (4) describes solid phase concentration along the radius of each spherical particle of active material, the macroscopic model requires only the concentration at the surface, $c_{s,e}(t)$, as a function of the time history of local reaction current density, $j^{Li}(t)$.

We transform the PDE, Eq. (4), from spherical to planar coordinates using the substitution $v(r) = rc_s(r)$ [28,29] and discretize the transformed equation in the $r$-direction with $n$ linear elements. (The present model uses five elements with node points placed at $\{0.7, 0.91, 0.97, 0.99, 1.0\} \times R_s$.) Transformed back to spherical coordinates, the discretized system is represented as ODEs in state space form:

$$\begin{bmatrix} \dot{c}_{s,1} \\ \dot{c}_{s,2} \\ \vdots \\ \dot{c}_{s,n} \end{bmatrix} = \mathbf{A} \begin{bmatrix} c_{s,1} \\ c_{s,2} \\ \vdots \\ c_{s,n} \end{bmatrix} + \mathbf{B} j^{Li}, \qquad c_{s,e} \approx \mathbf{C} \begin{bmatrix} c_{s,1} \\ c_{s,2} \\ \vdots \\ c_{s,n} \end{bmatrix} + \mathbf{D} j^{Li}, \tag{A.1}$$

where the $n$ states of the system are the radially distributed values of concentration $c_{s,1}, \ldots, c_{s,n}$, at finite element node points $1, \ldots, n$. For the linear PDE (4) with constant diffusion coefficient, $D_s$, the matrix $\mathbf{A}$ is constant and tri-diagonal.

The linear state space system (A.1) can also be expressed as a transfer function:

$$\frac{c_{s,e}(s)}{j^{Li}(s)} \approx G(s) = \frac{b_1 s^n + b_2 s^{n-1} + \cdots + b_{n-1} s + b_n}{a_1 s^n + a_2 s^{n-1} + \cdots + a_{n-1} s + a_n} \tag{A.2}$$

with constant coefficients $a_i$ and $b_i$ [30]. While either (A.1) or (A.2) could be numerically implemented using an iterative solution method, we exploit the linear structure of (4) and express the system as a finite difference equation with explicit solution. To discretize (A.2) with respect to time, we perform a $z$-transform using Tustin's method:

$$G_T(z) = G(s)|_{s=(2/T_s)((z-1)/(z+1))}, \tag{A.3}$$

resulting in an $n$th-order discrete transfer function:

$$\frac{c_{s,e}(z)}{j^{Li}(z)} \approx G_T(z) = \frac{h_1 z^n + h_2 z^{n-1} + \cdots + h_{n-1} z + h_n}{g_1 z^n + g_2 z^{n-1} + \cdots + g_{n-1} z + g_n} \tag{A.4}$$

with constant coefficients $h_i$ and $g_i$. Computation is thus reduced to an explicit algebraic formula with minimal memory requirements. Solution for $c_{s,e}$ requires that local values of $c_{s,e}$ and $j^{Li}$ be held from only the previous $n-1$ time steps.

## Appendix B

### B.1. Transfer functions of short and long time solid-state diffusion analytical solutions

Doyle et al. [11] employ an analytical solution to Eq. (4) and embed it inside a Duhamel superposition integral to accommodate the time dependent boundary condition. They provide two integral expressions for the response of reaction current, $j^{Li}(\tau)$, to a step in surface concentration, $\Delta c_{s,e}$, at $\tau = 0$, each in the form

$$a(\tau) = \frac{1}{a_s F} \frac{R_s}{D_s} \frac{1}{\Delta c_{s,e}} \int_0^\tau j^{Li}(\zeta)\, d\zeta. \tag{B.1}$$

The short time expression (Eq. (B.6) of [11]) is

$$a(\tau) = -\tau + 2\sqrt{\frac{\tau}{\pi}} \left[ 1 + 2 \sum_{n=1}^{\infty} \exp\left(-\frac{n^2}{\tau}\right) - n\sqrt{\frac{\pi}{\tau}}\, \mathrm{erfc}\left(\frac{n}{\sqrt{\tau}}\right) \right], \tag{B.2}$$

while the long time expression (Eq. (B.5) of [11]) is

$$a(\tau) = \frac{2}{\pi^2}\sum_{n=1}^{\infty}\frac{1}{n^2}[1-\exp(-n^2\pi^2\tau)]. \tag{B.3}$$

Little detail is given in the derivation of these expressions. Differentiating Eqs. (B.1)–(B.3) with respect to $\tau$ and solving for $j^{\mathrm{Li}}(\tau)$, we recover short time solution:

$$j^{\mathrm{Li}}(\tau) = a_s F\frac{D_s}{R_s}\left[1-\frac{1}{\sqrt{\pi\tau}}+\frac{2}{\sqrt{\pi\tau}}\sum_{n=1}^{\infty}\exp\left(-\frac{n^2}{\tau}\right)\right]\Delta c_{s,e} \tag{B.4}$$

and long time solution:

$$j^{\mathrm{Li}}(\tau) = a_s F\frac{D_s}{R_s}\left[-2\sum_{n=1}^{\infty}\exp(-n^2\pi^2\tau)\right]\Delta c_{s,e} \tag{B.5}$$

no longer in integral form. Taking the Laplace transform of Eqs. (B.4) and (B.5) and recognizing that the transform of the step input is $C_{s,e}(s) = \Delta c_{s,e}/s$, we find the short time transfer function:

$$\frac{J^{\mathrm{Li}}(s)}{C_{s,e}(s)} = a_s F\frac{D_s}{R_s}\left[1-R_s\sqrt{\frac{s}{D_s}}+2R_s\sqrt{\frac{s}{D_s}}\sum_{n=1}^{\infty}\times\exp\left(-2nR_s\sqrt{\frac{s}{D_s}}\right)\right] \tag{B.6}$$

and the long time transfer function:

$$\frac{J^{\mathrm{Li}}(s)}{C_{s,e}(s)} = a_s F\frac{D_s}{R_s}\left[-2\sum_{n=1}^{\infty}\frac{s}{s+n^2\pi^2}\right]. \tag{B.7}$$

Taking the reciprocal of Eqs. (B.6) and (B.7) and substituting dimensionless variables $\bar{J}^{\mathrm{Li}}$, $\bar{C}_{s,e}$, and $\psi$ yields Eqs. (25) and (26) respectively, used in Section 4.4.

## Appendix C

### *C.1. Transfer function of parabolic profile solid-state diffusion approximate model*

Wang et al. [19] assume concentration distribution within a spherical active material particle to be described by a parabolic profile. Integrating the two parameter polynomial with respect to Eq. (4), they reduce the problem of determining surface concentration, $c_{s,e}(t)$, as a function of reaction current, $j^{\mathrm{Li}}(t)$, down to the solution of one ODE:

$$\frac{\partial c_{s,\mathrm{avg}}}{\partial t} = \frac{3}{a_s F R_s}j^{\mathrm{Li}} \tag{C.1}$$

and one interfacial balance:

$$c_{s,e} - c_{s,\mathrm{avg}} = \frac{R_s}{5a_s F D_s}j^{\mathrm{Li}}. \tag{C.2}$$

Taking the Laplace transform of Eqs. (C.1) and (C.2) yields:

$$sC_{s,\mathrm{avg}}(s) = \frac{3}{a_s F R_s}J^{\mathrm{Li}}(s) \tag{C.3}$$

and

$$C_{s,e}(s) - C_{s,\mathrm{avg}}(s) = \frac{R_s}{5a_s F D_s}J^{\mathrm{Li}}(s), \tag{C.4}$$

which when combined to eliminate $C_{s,\mathrm{avg}}$, provides the transfer function:

$$\frac{C_{s,e}(s)}{J^{\mathrm{Li}}(s)} = \frac{1}{a_s F}\frac{R_s}{D_s}\left[\frac{3D_s}{sR_s^2}+\frac{1}{5}\right]. \tag{C.5}$$

Substituting dimensionless variables $\bar{J}^{\mathrm{Li}}$, $\bar{C}_{s,e}$, and $\psi$ into Eq. (C.5) yields Eq. (27), used in Section 4.4.

## References


[1] M. Doyle, J. Newman, A.S. Gozdz, C.N. Schmutz, J.M. Tarascon, J. Electrochem. Soc. 143 (1996) 1890–1903.
[2] M. Doyle, Y. Fuentes, J. Electrochem. Soc. 150 (2003) A706–A713.
[3] W.B. Gu, C.Y. Wang, ECS Proc. 99-25 (2000) 748–762.
[4] FreedomCAR Battery Test Manual For Power-Assist Hybrid Electric Vehicles, DOE/ID-11069, 2003.
[5] P. Nelson, I. Bloom, K. Amine, G. Hendriksen, J. Power Sources 110 (2002) 437–444.
[6] S. Al Hallaj, H. Maleki, J. Hong, J. Selman, J. Power Sources 83 (1999) 1–8.
[7] P. Nelson, D. Dees, K. Amine, G. Henriksen, J. Power Sources 110 (2002) 349–356.
[8] E. Karden, S. Buller, R. DeDoncker, Electrochem. Acta 47 (2002) 2347–2356.
[9] S. Barsali, M. Ceraolo, Electrochem. Acta 47 (2002) 2347–2356.
[10] J. Christophersen, D. Glenn, C. Motloch, R. Wright, C. Ho, Proceedings of the IEEE Vehicular Technology Conference, vol. 56, Vancouver, Canada, 2002, pp. 1851–1855.
[11] M. Doyle, T. Fuller, J. Newman, J. Electrochem. Soc. 140 (1993) 1526–1533.
[12] M. Doyle, T. Fuller, J. Newman, Electrochem. Acta 39 (1994) 2073–2081.
[13] T. Fuller, M. Doyle, J. Newman, J. Electrochem. Soc. 141 (1994) 1–10.
[14] T. Fuller, M. Doyle, J. Newman, J. Electrochem. Soc. 141 (1994) 982–990.
[15] I. Ong, J. Newman, J. Electrochem. Soc. 146 (1999) 4360–4365.
[16] M. Doyle, J. Meyers, J. Newman, J. Electrochem. Soc. 147 (2000) 99–110.
[17] J. Meyers, M. Doyle, R. Darling, J. Newman, J. Electrochem. Soc. 147 (2000) 2930–2940.
[18] P. Arora, M. Doyle, R. White, J. Electrochem. Soc. 146 (1999) 3543–3553.
[19] C.Y. Wang, W.B. Gu, B.Y. Liaw, J. Electrochem. Soc. 145 (1998) 3407.
[20] V. Subramanian, J. Ritter, R. White, J. Electrochem. Soc. 148 (2001) E444–E449.
[21] K. Smith, C.Y. Wang, J. Power Sources 160 (2006) 662–673.
[22] L.O. Valøen, J.N. Reimers, J. Electrochem. Soc. 152 (2005) A882–A891.
[23] D. Dees, E. Gunen, D. Abraham, A. Jansen, J. Prakash, J. Electrochem. Soc. 152 (2005) A1409–A1417.
[24] C.Y. Wang, V. Srinivasan, J. Power Sources 110 (2002) 364–376.
[25] H.S. Carslaw, J.C. Jaeger, Conduction of Heat in Solids, Oxford University Press, London, 1973, p. 112.
[26] K. Smith, C.Y. Wang, Proceedings of the SAE Future Transportation Technology Conference, Chicago, IL, September 7–9, 2005.
[27] G. Sikha, R.E. White, B.N. Popov, J. Electrochem. Soc. 152 (2005) A1682–A1693.
[28] T. Jacobsen, K. West, Electrochem. Acta 40 (1995) 255–262.
[29] M.N. Özişik, Heat Conduction, John Wiley & Sons, New York, 1993, pp. 327–334.
[30] G. Franklin, J.D. Powell, M. Workman, Digital Control of Dynamic Systems, 3rd ed., Addison-Wesley/Longman, Menlo Park, CA, 1998.